

# Unexpected secondary flows in reverse nonequilibrium shear flow simulations

Antonia Statt,<sup>\*</sup> Michael P. Howard,<sup>†</sup> and Athanassios Z. Panagiotopoulos

*Department of Chemical and Biological Engineering,  
Princeton University, Princeton, New Jersey 08544, USA*

## Abstract

We simulated two particle-based fluid models, namely multiparticle collision dynamics and dissipative particle dynamics, under shear using reverse nonequilibrium simulations (RNES). In cubic periodic simulation boxes, the expected shear flow profile for a Newtonian fluid developed, consistent with the fluid viscosities. However, unexpected secondary flows along the shear gradient formed when the simulation box was elongated in the flow direction. The standard shear flow profile was obtained when the simulation box was longer in the shear-gradient dimension than the flow dimension, while the secondary flows were always present when the flow dimension was at least 25% larger than the shear-gradient dimension. The secondary flows satisfy the boundary conditions imposed by the RNES and have a lower rate of viscous dissipation in the fluid than the corresponding unidirectional flows. This work highlights a previously unappreciated limitation of RNES for generating shear flow in simulation boxes that are elongated in the flow dimension, an important consideration when applying RNES to complex fluids like polymer solutions.

---

<sup>\*</sup> astatt@princeton.edu

<sup>†</sup> mphoward@utexas.edu; Present address: McKetta Department of Chemical Engineering, University of Texas at Austin, Austin, Texas 78712, USA

## I. INTRODUCTION

The reverse nonequilibrium simulation method (RNES) developed by Müller-Plathe [1, 2] is a well established technique for computing transport coefficients of particle-based fluid models. It was initially proposed as a method to determine thermal conductivity [1] and was later extended to the shear viscosity [2]. RNES has been used to calculate the thermal conductivity of simple liquids [1, 3], salts [4], carbon nanotubes [5, 6], and silicon [7]; to study the Ludwig–Soret effect [3, 8]; and to measure the shear viscosities of simple fluids [9], polymer solutions and melts [10–12], ionic liquids [13], alcohols [14], and water [15]. RNES has also been successfully applied to more complex systems under shear, including colloidal suspensions of nanoparticles [16–20], surfactant solutions [21], and asphalt [22]. More recently, RNES was used not only to compute transport properties, but also to investigate dynamic phenomena like the shear-induced reorientation of diblock-copolymer lamellae [23] and the aggregation of patchy particles in flow [24].

The underlying idea of RNES is to impose an “effect” on a system in an unphysical way and measure the “cause”. In many nonequilibrium simulation techniques, a gradient (cause) is imposed and a flux (effect) is measured [25], but RNES reverses this picture. For example, in RNES, stress can be generated by an unphysical transfer of momentum between particles [2], driving the system out of equilibrium and resulting in a physical momentum flux. The stress gives rise to a corresponding flow profile that can be measured. Given an imposed flux and measured gradient, the relevant transport coefficient (e.g., shear viscosity) can be extracted within the linear-response regime.

RNES possesses many desirable properties of a nonequilibrium method [1, 26]. It is quickly converging compared to equilibrium methods, such as the Green–Kubo relations [27], to determine transport coefficients. RNES is compatible with a multitude of different particle-based models. It also does not require a specific simulation box geometry and accommodates periodic boundary conditions, which eliminates artificial wall effects that could cause measured fluid properties to differ from the bulk in small, wall-bounded simulation boxes [28]. Additionally, RNES can be made to conserve momentum and energy and acts as its own thermostat [26], avoiding the challenges of applying an external thermostat out of equilibrium [29]. Because of its straightforward implementation and flexibility, RNES is widely used and is implemented in many simulation packages, including LAMMPS [30],

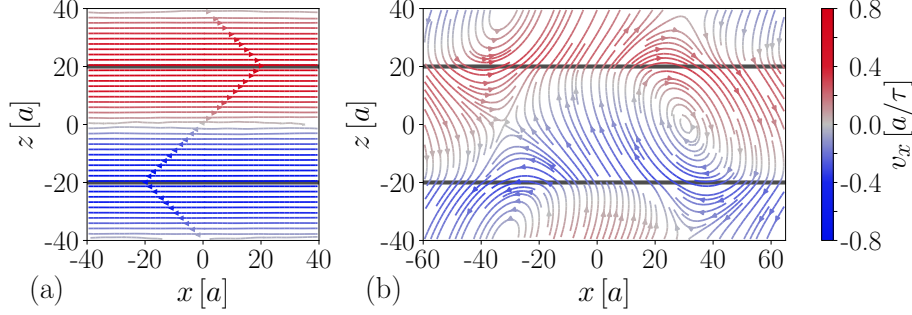


FIG. 1. Streamlines in the  $xz$ -plane for the flow induced by RNES in (a) a cubic box ( $80a \times 80a \times 80a$ ) and (b) an orthorhombic box ( $125a \times 80a \times 80a$ ). Color indicates the  $x$ -component of the velocity,  $v_x$ . Gray horizontal lines mark the exchange slabs of width  $w = 1a$  at  $z = \pm 20a$ .

HOOMD-blue [31], OPENMD [32], and ESPResSo [33].

Despite these many positive attributes, we have uncovered a previously unappreciated limitation of RNES for simulating shear flow. We applied RNES to two different model fluids in various simulation box geometries. Unexpectedly, we not only obtained the standard shear flows (Fig. 1a), but also more complicated flow patterns (Fig. 1b) in certain non-cubic boxes with periodic boundary conditions. In those cases, the flow had significant secondary components along the shear gradient, and the shear stress did not have constant magnitude throughout the system. Such flows are undesirable because they severely complicate the calculation of the shear viscosity using RNES.

In this article, we systematically interrogated the flow field, stress, and viscous dissipation as functions of the simulation box geometry and the shear rate to determine *why* and *when* RNES did not generate the expected shear flow. We show that the secondary flows emerge due to the periodic boundary conditions and are not specific to the RNES method for generating shear flow, suggesting a hydrodynamic instability inherent to the flow and geometry. The rest of the article is organized as follows. The RNES algorithm and its known properties and features are explained in Sec. II. The simulation details and fluid models are described in Sec. III. Our results are presented and discussed in Sec. IV and are followed by our conclusions in Sec. V.

## II. RNES ALGORITHM

We first summarize details of the RNES algorithm for simulating shear flow and its known features and limitations. The simulation box is defined to be of size  $L_x \times L_y \times L_z$ , with  $x$  being the direction of flow and  $z$  being the direction of the shear gradient (Fig. 2). The box is periodic in all three dimensions. In the standard RNES algorithm for generating shear flow [2], two exchange slabs of width  $w$  are constructed at  $z = \pm L_z/4$ . At regular intervals  $\Delta t$  during the simulation, pairs of particles are selected from the slabs and their momenta are swapped. The particle with the most negative momentum in the flow direction,  $p_x^-$ , is selected from the upper slab, while the particle with the most positive  $x$ -momentum,  $p_x^+$ , is chosen from the lower slab. An unphysical swap move exchanges  $p_x^-$  and  $p_x^+$ , resulting in a transfer of momentum  $\Delta p_x = p_x^+ - p_x^-$ . The exchange of momentum generates a physical momentum flux with a corresponding shear stress,  $\tau_{zx}$ , at steady state [2]:

$$\tau_{zx} = \frac{\langle \Delta p_x \rangle}{2L_x L_y \Delta t}. \quad (1)$$

Here,  $\langle \Delta p_x \rangle$  denotes the average amount of momentum exchanged during the interval  $\Delta t$ , and the factor of 2 is due to the periodic boundary conditions. If both particles in the swapped pair have the same mass, the total momentum and kinetic energy of the system are conserved during the momentum transfer.

The imposed stress is expected to generate a flow field  $\mathbf{v}$ . Assuming the steady, incompressible flow of a Newtonian fluid, the standard continuity equation and momentum balances governing the flow are [34]

$$\nabla \cdot \mathbf{v} = 0 \quad (2)$$

$$\rho \mathbf{v} \cdot \nabla \mathbf{v} = -\nabla p + \nabla \cdot \boldsymbol{\tau}, \quad (3)$$

where  $\rho$  is the density,  $p$  is the pressure, and  $\boldsymbol{\tau} = \mu(\nabla \mathbf{v} + (\nabla \mathbf{v})^T)$  is the viscous stress tensor with  $\mu$  being the shear viscosity. We approximate the exchange procedure by a constant shear stress  $\tau_{zx}$  at the center of the exchange regions ( $z = \pm L_z/4$ ) and a uniform pressure, which implies that there is no flow in  $y$  or  $z$ . Applying the periodic boundary conditions of

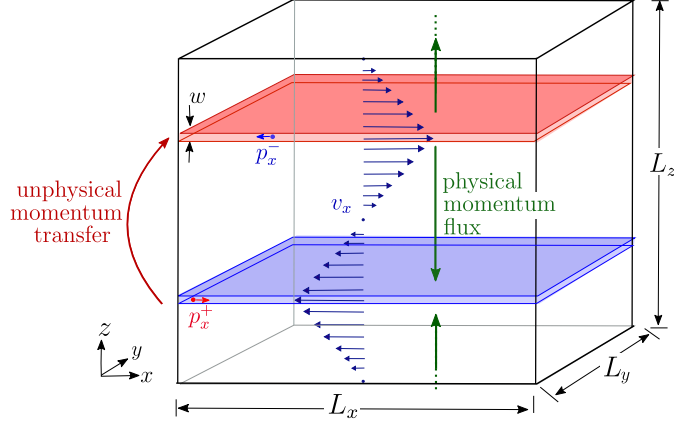


FIG. 2. Sketch of the simulation box of dimensions  $L_x \times L_y \times L_z$ , where  $x$  is the flow direction and  $z$  is the gradient direction. The two exchange slabs of width  $w$  are located at  $-L_z/4$  (bottom, blue) and  $+L_z/4$  (top, red). Unphysical momentum swaps between pairs occur in the top and bottom slab, driving a shear-induced physical momentum flux back (green). The expected velocity field given by eq. 4,  $v_x(z)$ , is sketched in blue.

the simulation box gives the steady-state shear flow field,  $v_x(z)$ ,

$$v_x(z) = \begin{cases} \dot{\gamma}(-L_z/2 - z), & z < -L_z/4 \\ \dot{\gamma}z, & |z| < L_z/4 \\ \dot{\gamma}(L_z/2 - z), & z > L_z/4 \end{cases}, \quad (4)$$

where  $\dot{\gamma} = \tau_{zx}/\mu$  is the shear rate in this geometry. This flow field is illustrated in Fig. 2. Note that due to the periodic boundary conditions, the standard Couette flow ( $|z| < L_z/4$ ) is extended outside the exchange regions, resulting in an overall triangular profile. In RNES, the width of the exchange regions  $w$  should be as small as possible to minimally disturb this expected flow field [23], while still keeping the regions large enough to contain a sufficient number of swapping pairs.

The imposed shear stress can be used to determine the shear viscosity  $\mu$  from the measured flow field within the linear-response regime,

$$\tau_{zx} = \mu \left\langle \frac{\partial v_x}{\partial z} \right\rangle = \begin{cases} \mu \dot{\gamma}, & |z| < L_z/4 \\ -\mu \dot{\gamma}, & |z| > L_z/4 \end{cases}. \quad (5)$$

The shear rate  $\dot{\gamma}$  can be varied by tuning the momentum exchange rate to change  $\tau_{zx}$ , and  $\mu$  is usually extracted from a series of measurements at different  $\dot{\gamma}$ . RNES has technical

limitations at both very low and very high shear rates. For low shear rates, infrequent momentum swaps may not lead to a steady flow profile [35, 36]. Analogous problems have been reported for the determination of thermal coefficients using RNES [7]. As suggested in Ref. 36, this issue can be partially alleviated with a weaker, more frequent exchange of momentum, e.g., by choosing pairs with momenta close to a target value instead of the maximum [35]. This modification allows the flow rate to be tuned more precisely [35, 37], and also leads to a weaker system-size dependence and better convergence of the measured viscosity [37]. For high shear rates, the velocities in the exchange regions deviate from the expected Boltzmann distributions [35]. The velocity distribution in the lower slab develops a shoulder towards lower values, whereas the distribution in the upper slab develops a shoulder towards higher values because the imposed momentum transfer exceeds the system’s ability to thermalize. In this case, RNES significantly underpredicts viscosities relative to other computational methods [35]. The numerical bounds on the accessible shear rates depend on the fluid model and must be determined carefully by trial and error.

The RNES algorithm does not specify a box size or shape, and different geometries have been chosen by different authors. For example, Müller-Plate [1] originally used a box that was three times longer in the gradient direction than in the flow direction ( $L_z = 3L_x$ ). Nikoubashman and Howard chose  $L_z = L_x$  to simulate polymer solutions in shear [11], while Schneider et al. utilized boxes with  $L_z = 2L_x - 4.6L_x$  to study reorientation of diblock copolymers melts [23]. Generally, and as is standard in molecular simulations [38], the simulation box must be large enough in all dimensions to avoid unphysical self-interactions through periodic boundaries, particularly between macromolecules like polymers. Since many macromolecules align and stretch with the flow [39], the simulation box can similarly be expanded along the flow dimension to match the expected deformation ( $L_x > L_z$ ). This geometry reduces the overall computational cost of the simulation compared to expanding the box in all dimensions. However, as we will show in Sec. IV, elongating the box in the flow dimension has previously unknown and undesirable consequences for RNES.

### III. SIMULATION MODELS

We applied RNES to simulate shear flow for two fluids, one modeled using multiparticle collision dynamics (MPCD) [40, 41] and the other using dissipative particle dynamics (DPD)

[42–44]. Both MPCD and DPD are particle-based mesoscale models that faithfully resolve hydrodynamic interactions and incorporate the effects of thermal fluctuations [45]. In this article, we will describe the model parameters and our results using  $a$  as the unit of length,  $\varepsilon$  as the unit of energy, and  $m$  as the unit of mass. In this system of units,  $\tau = \sqrt{ma^2/\varepsilon}$  is the unit of time.

The MPCD fluid consisted of point-like particles of mass  $m$ . The particle positions and velocities were propagated in alternating streaming and collision steps [40, 41]. Particles moved ballistically during the streaming step and were subsequently binned into cubic cells of size  $a$ . The particle coordinates were collectively shifted by a random value between  $\pm a/2$  during binning to ensure Galilean invariance [46, 47]. In the ensuing collision step, the particle velocities relative to the cell-average velocity were rotated by a fixed angle  $\alpha$  around an axis randomly chosen from the unit sphere for each cell. This collision procedure, also called stochastic rotation dynamics, conserves linear momentum in each cell. Because of the local momentum conservation, it also conserves linear momentum globally.

The properties of the MPCD fluid are controlled by the particle number density, the rotation angle, the temperature, and the time between collisions [40, 41, 48]. We chose the density as  $\rho = 5 a^{-3}$  and the rotation angle as  $\alpha = 130^\circ$ , and performed a collision every  $0.1 \tau$ . We additionally applied a Maxwell–Boltzmann rescaling thermostat [49, 50] to each cell to maintain a constant temperature  $T = 1.0 \varepsilon/k_B$  throughout the fluid, where  $k_B$  is Boltzmann’s constant. Since a thermostat is not required in RNES, we confirmed that removing the thermostat did not qualitatively change our results. The viscosity  $\mu$  can be estimated for the MPCD fluid using kinetic theory [51], giving  $\mu = 3.96 \varepsilon \tau / a^3$  for our parameters.

The DPD fluid [42, 52] was also represented by particles of mass  $m$ . A conservative force, a dissipative force, and a random force acted between pairs of particles within a distance  $r_c$  of each other. The dissipative and random forces were consistent with the fluctuation–dissipation theorem and conserved local momentum. Details of the functional forms of the DPD interactions can be found in Ref. 44. We employed standard parameters: a maximum conservative force of  $25 \varepsilon / a$ , a drag coefficient of  $4.5 m / \tau$  for the dissipative force, a cutoff of  $r_c = 1 a$ , and an integration time step of  $0.01 \tau$  [44]. The particle number density was  $\rho = 3 a^{-3}$  [44, 53], and the temperature was  $T = 1.0 \varepsilon / k_B$ .

We determined the viscosity of the DPD fluid for our parameters using RNES in cubic

boxes with edge lengths ranging from  $25a$  to  $65a$ , finding  $\mu = 0.87 \varepsilon \tau / a^3$ . We independently validated the RNES measurement using the periodic Poiseuille flow method [54]. We divided the simulation box into two domains with  $z < 0$  and  $z \geq 0$  and applied a constant body force with equal magnitude but opposite direction ( $\pm x$ ) between the regions. We extracted the viscosity by fitting the velocity profile to the expected parabolic form [54]. The obtained value of  $\mu = 0.87 \varepsilon \tau / a^3$  was in good agreement with the RNES measurement and values reported elsewhere [55].

All simulations were performed on graphics processing units using HOOMD-blue (version 2.1.1) [31, 56–58] with our own implementation of RNES. We additionally reproduced selected results for the MPCD fluid using another implementation [59] and for the DPD fluid using LAMMPS (11 Aug 2017) [30, 60]. An example LAMMPS script for simulating the DPD fluid is included as supplemental material [61].

#### IV. RESULTS AND DISCUSSION

We first simulated the MPCD fluid in two boxes: a cubic box of size  $80a \times 80a \times 80a$  and an orthorhombic box, elongated along the flow direction, of size  $125a \times 80a \times 80a$ . The slab exchange width was  $w = 1a$ , and the swapped particles were chosen to have momenta closest to a target value of  $\pm 0.5ma/\tau$ . We swapped 202 pairs in the cubic box and 316 pairs in the orthorhombic box every step, resulting in the same imposed stress ( $\tau_{zx} = 0.158 \varepsilon / a^3$ ) for both boxes. The cubic box developed the expected triangular velocity profile (eq. 4) with extrema in the exchange regions (Fig. 1a). No flows occurred in either of the other directions ( $v_y = v_z = 0$ ). We extracted a viscosity of  $\mu = 3.95 \varepsilon \tau / a^3$  from the measured flow field using eq. 5, in quantitative agreement with the viscosity estimated from kinetic theory.

We expected that applying the RNES method in the orthorhombic box should result in the same velocity profile because the same stress was applied; surprisingly, a markedly different flow field developed (Fig. 1b). The average velocity in the exchange regions was still along  $x$  as expected, but substantial flows along the shear gradient ( $z$ ) were also obtained, giving an overall two-dimensional flow field ( $v_y$  remained zero). A movie of the three-dimensional streamlines as they develop from a quiescent fluid can be found in the supplemental material [61]. The resulting streamlines exhibited two vortices and two stagnation points, with one of each between the exchange slabs. The vortices and stagnation



points were stationary during the accessible simulation time. The DPD fluid under shear had the same qualitative behavior as the MPCD fluid, indicating that this surprising flow field is not specific to the MPCD model. We have extensively tested and verified that the momentum exchanged between the slabs is in agreement with the expected value in all simulated systems and that all flow fields satisfy the continuity equation (eq. 2). An example of this calculation can be found in Fig. S1 [61].

One possible explanation for the presence of vortices in the flow could be the emergence of turbulence in the Couette flow. To estimate this effect, we defined a Reynolds number  $\text{Re} = \rho U L_z / 4\mu$  based on the maximum velocity in the exchange slabs  $U$  and the half-width between the exchange slabs,  $L_z/4$ . It has been shown that the transition from laminar to turbulent flow in planar Couette flow can occur for Reynolds numbers as low as  $\text{Re} \approx 300$  [62–64]. For Fig. 1a, the Reynolds number is  $\text{Re} \approx 20$ , which is well-below the laminar–turbulent transition for the classical Couette flow. Expanding the box along  $x$  does not change  $\text{Re}$ , and so turbulence based on the flow is not expected for the orthorhombic box either. To exclude possible finite-size effects, we performed a simulation in a box of size  $125a \times 80a \times 125a$  at  $\text{Re} = 20$  as well as at  $\text{Re} = 50$  and obtained only flows like Fig. 1a.

As an additional stability test, we introduced two vortices and two stagnation points into a cubic box ( $80a \times 80a \times 80a$ ) and followed the evolution of the flow. The vortices dissipated completely after  $70000\tau$  and the flow returned to the expected triangular flow profile. This shows that the expected shear flow is not metastable with respect to the vortices for the cubic box. Likewise, we initialized the expected shear flow in an orthorhombic box ( $125a \times 80a \times 80a$ ) and observed the emergence of vortices from the triangular flow on a similar timescale. The final steady state was independent of how the fluid was initialized for both box shapes.

One of the benefits of using the RNES method is the ability to readily compute the shear viscosity from simulations from a simple shear flow profile (eq. 5). The secondary flows in the orthorhombic box effectively prevent this calculation and are undesirable for simulating simple shear. In the next sections, we investigate the local shear stress (Sec. IV A), the effect of boundary conditions (Sec. IV B), and the viscous dissipation in the fluid (Sec. IV C) to understand when and why the secondary flows appear so that they can be avoided.

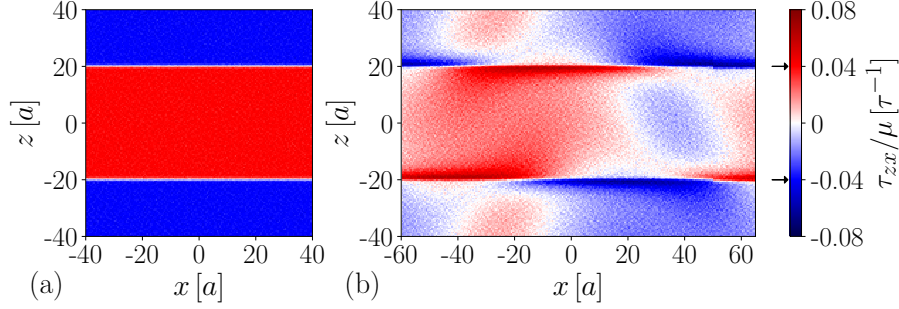


FIG. 3. Local shear stress  $\tau_{zx}/\mu$  in the fluid in (a) a cubic box and (b) an orthorhombic box for the flow fields of Fig. 1. The expected values based on eq. 5,  $\tau_{zx}/\mu = \pm 0.04 \tau^{-1}$ , are indicated by arrows on the color bar.

### A. Shear Stress

In deriving the expected shear flow field (eq. 4), we assumed that the shear stress in the exchange regions was constant and equal to the value imposed by RNES. In order to test this assumption, we computed the viscous stress tensor  $\boldsymbol{\tau}$  from the measured flow fields. Fig. 3 shows the shear stress,  $\tau_{zx}$ , corresponding to the flows in Fig. 1. The cubic box (Fig. 3a) exhibited the expected step function behavior (eq. 5),  $\tau_{zx}/\mu = \pm 0.04 \tau^{-1}$ . Only the exchange regions of width  $w = 1 a$  at  $z = \pm 20 a$  deviated from the expected values, showing a shear stress close to zero. This is not surprising because the stress in the fluid should vary continuously. In contrast, the shear stress in the orthorhombic box (Fig. 3b) was strongly position dependent. The shear stress was lower near the vortices and stagnation points, but exhibited localized areas of significantly higher stress close to the exchange regions.

In order to confirm that the width of the exchange region  $w$  did not significantly affect the viscous stress, we systematically decreased  $w$  for both the MPCD and DPD fluids. Since the number of possible pairs to swap decreased with  $w$ , we chose a lower target shear stress than in Fig. 3, using  $\tau_{zx} = 0.068 \varepsilon/a^3$  for MPCD and  $\tau_{zx} = 0.015 \varepsilon/a^3$  for DPD, which gives an expected shear rate of  $\dot{\gamma} = 0.0172 \tau^{-1}$  for both fluids. The computed shear stress was averaged over  $x$  to give the average stress,  $\langle \tau_{zx} \rangle$ , as a function of  $z$ .

For the cubic box (Fig. 4a),  $\langle \tau_{zx} \rangle$  was again a step function for both fluids outside the exchange regions, as expected, regardless of the width of the exchange region, but some deviations were observed near the exchange regions. The stress profile for the MPCD fluid was rounded and increased in steepness with decreasing  $w$ , whereas the shear stress in the

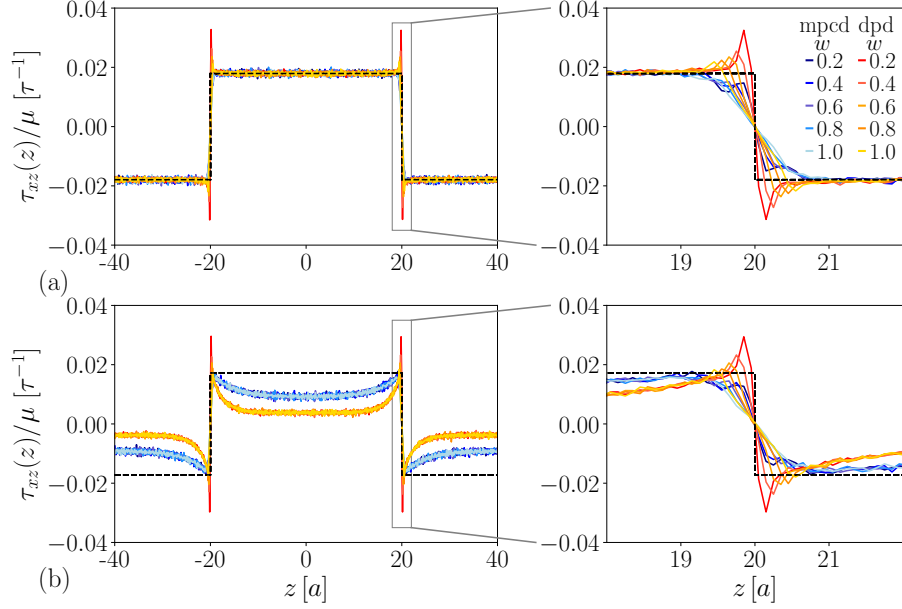


FIG. 4. Average shear stress  $\langle \tau_{zx} \rangle$  in (a) a cubic box ( $80a \times 80a \times 80a$ ) and (b) an orthorhombic box ( $125a \times 80a \times 80a$ ) for the MPCD and DPD fluids. The width  $w$  of the exchange region was varied from  $0.2a$  to  $1.0a$  as indicated in the legend. The expected step function,  $\tau_{zx}/\mu = \pm 0.0172 \tau^{-1}$ , is shown as a dashed line.

DPD fluid overshoot the expected value close to the exchange region by an amount that increased with decreasing  $w$ . The overshoot in shear stress corresponds to the velocity being larger than expected near the exchange region, which is consistent with previous simulations of DPD models [23]. The rounded stress profile for the MPCD fluid is similarly consistent with rounding of the velocity profile in the exchange region that has been reported elsewhere [19].

For the orthorhombic box (Fig. 4b), both fluids showed a significant reduction in  $\langle \tau_{zx} \rangle$  outside the exchange regions compared to the cubic box. As for the cubic box, the exchange region width again did not influence the value of the stress in these regions. Also consistent with the cubic box, the DPD fluid had stress overshoot in the exchange region, whereas the MPCD fluid had a rounded profile. Most significantly, we note that  $\langle \tau_{zx} \rangle$  in the exchange regions was essentially indistinguishable between the cubic and orthorhombic boxes. Although the shear stress in the exchange regions of the orthorhombic box was not *constant*, the RNES algorithm still imposed the same *average* stress in the exchange regions for both simulation boxes.

## B. Boundary Conditions

Our shear stress measurements suggest that the RNES method imposes boundary conditions that are inconsistent with the assumptions used to derive eq. 4: namely, a constant shear stress  $\tau_{zx}$  at  $z = \pm L_z/4$  and a unidirectional flow ( $v_y = v_z = 0$ ). In the previous section, we showed that RNES imposes the average shear stress in the exchange regions. This is a weaker boundary condition than a constant stress and does not enforce that  $v_z = 0$ . Clearly,  $v_z \neq 0$  for the orthorhombic box (Fig. 1b).

To test the influence of including the condition that  $v_z = 0$  in RNES, we inserted two smooth, hard walls into the orthorhombic box just outside the exchange regions, effectively simulating half of the system ( $|z| < L_z/4$ ). We performed this test only for the MPCD fluid, which does not exhibit local structuring near a wall. The MPCD particles were reflected from the hard wall using bounce-back reflections for a slip boundary condition. The walls enforce that  $v_z = 0$  since the fluid cannot penetrate the hard surface, but the slip boundary condition does not modify the flow tangent to the surface. We then applied the RNES momentum exchange to the fluid. We found that only the expected shear flow,  $v_x(z)$ , formed between the exchange regions, even in boxes with  $L_z > L_x$ , as shown in Fig. 5b. From this test, we conclude that secondary flows only form in RNES for fully periodic boxes that are subject to an average stress boundary condition but do not constrain  $v_z = 0$ .

Because the previous test restricted the flow field to only one half of the RNES with periodic boundary conditions, we also inserted two smooth, hard no-slip walls at exactly  $z = \pm L_z/2$ , effectively replacing the periodic boundary condition in one dimension while keeping the rest of the system unchanged. We included virtual MPCD particles [65, 66] at random positions in the walls with velocities drawn from the Maxwell-Boltzmann distribution to help enforce the no-slip condition. In this case, the entire flow field given by eq. 4 is recovered, as shown in Fig. 5c. To test possible finite size effects, we repeated the simulation in a box twice as big in  $x$  and  $z$  dimension and did not observe a difference in flow behavior.

To test whether the secondary flows are due to the RNES momentum exchange procedure for generating the flow (average stress condition), we considered an alternative nonequilibrium scheme. We applied constant opposite body forces to all particles in the exchange regions instead of the usual RNES momentum exchange method. Here, we applied a force  $+\Delta f$  in the  $x$ -direction for each particle in the upper slab, and  $-\Delta f$  in the  $x$ -direction for

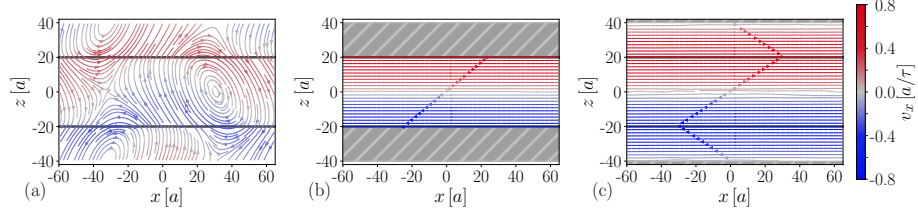


FIG. 5. Streamlines in the  $xz$ -plane for the flow induced by RNES in (a) an orthorhombic box ( $125a \times 80a \times 80a$ ) with periodic boundary conditions in all dimensions, (b) in the same box with slip walls placed at  $z = \pm 20.5a$ , and (c) in the same box with no-slip walls placed at  $z = \pm 40a$ . Color indicates the  $x$ -component of the velocity,  $v_x$ . Gray horizontal lines mark the exchange slabs of width  $w = 1a$  at  $z = \pm 20a$ .

each particle in the lower slab. While the method of generating the flow was different, the resulting flow profiles and stress distributions were identical to the ones observed by RNES. Together, these tests reveal that the observed behavior is not unique to the nonequilibrium method by which the flow is created, but rather appears to be an effect of the periodic boundary conditions.

### C. Viscous Dissipation

We have demonstrated that the unexpected secondary flows generated by RNES for simulation boxes that are elongated in the flow dimension are consistent with the continuity equation and average momentum flux imposed by RNES and appear to form due to the periodic boundary conditions in certain boxes. However, it is still unclear *when* and *why* a certain flow field is realized for a given simulation box. We use the total rate of viscous dissipation,  $\Phi$ , [34]

$$\Phi[\mathbf{v}(\mathbf{r})] = \int d\mathbf{r} \, \boldsymbol{\tau}[\mathbf{v}(\mathbf{r})] : \nabla \mathbf{v}(\mathbf{r}), \quad (6)$$

as an order parameter to detect the transition from the expected shear flow to the regime containing secondary flows. The rate of viscous dissipation is directly proportional to the rate of entropy production in an isothermal, incompressible flow [34, 67]. The expected viscous dissipation for the flow field given by eq. 4,  $\Phi_0$ , can be computed analytically as  $\Phi_0/V = \mu\dot{\gamma}^2$ , where  $V = L_x L_y L_z$  is the volume of the simulation cell.

To test if the rate of viscous dissipation detects the different flow profiles, we simulated

the MPCD and DPD fluids in rectangular boxes with aspect ratios varying from  $L_x/L_z = 0.5$  to 2.7. We performed the simulations at both a fixed shear stress and a fixed maximum velocity according to eq. 4. For the fixed shear stress simulations for the MPCD fluid, we varied  $L_y = L_z$  from  $80a$  to  $125a$ , and kept the area  $A = L_x L_y$  of the exchange region constant at  $A = 100^2 a^2$ . The DPD fluid simulations at fixed shear stress were performed in boxes with a exchange slab area of  $A = 50^2 a^2$  and varied  $L_z$  from  $30a$  to  $65a$ . For the fixed maximum velocity simulations we picked boxes with  $L_x = L_y = 100a$  and varied  $L_z$  from  $50a$  to  $125a$  for the MPCD fluid. Similarly, the DPD fluid simulations were performed in boxes with  $L_x = L_y = 50a$  and  $L_z$  from  $28a$  to  $60a$ . Averaged velocity profiles  $\langle v_x \rangle$  and  $\langle v_z \rangle$  can be found in Figs. S2 and S3 [61].

We then computed the total viscous dissipation  $\Phi$  from the measured flow fields using eq. 6. As demonstrated in Sec. IV A, the simulated flow field deviated from the theoretically expected profile near the exchange slabs even when no secondary flows occurred. To better facilitate comparison between the simulations and theory, we excluded the exchange slabs of size  $w = 1a$  from both the theoretical and numerical calculations of  $\Phi$ . We confirmed that neglecting these regions did not qualitatively change our findings, although it did lead to a small, constant shift of at most 5% in the reported values of  $\Phi$ .

We calculated the total viscous dissipation  $\Phi$  for both the MPCD and DPD fluids for various different box aspect ratios  $L_x/L_z$  at a constant average shear stress (Fig. 6a) and a constant maximum velocity, resulting in a varying shear stress (Fig. 6b). The viscous dissipation measured from the velocity gradients agreed with the theoretical predictions for all cases where the box aspect ratio was smaller than approximately  $L_x/L_z < 1.05$ . Above a critical value of approximately  $L_x/L_z > 1.25$ , the total viscous dissipation dropped significantly, concomitant with the emergence of secondary flows. The flow field that is realized in the simulation appears to minimize the total viscous dissipation.

We subsequently investigated the shear rate dependence of the secondary flows using  $\Phi$  as a parameter to identify the two different flow field types. We simulated both fluids at different momentum exchange rates in various box sizes and calculated  $\Phi$  (Fig. 7). We found that the system showed significant hysteresis effects for box aspect ratios  $L_x/L_z$  between 1.05 and 1.25. We initialized two simulations for each box geometry and shear rate: one with a flow field given by eq. 4 and the other with two vortices superimposed by an additional component  $v_z(x) \sim \cos(2\pi x/L_x)$ . For lower shear rates, the two different flows quickly

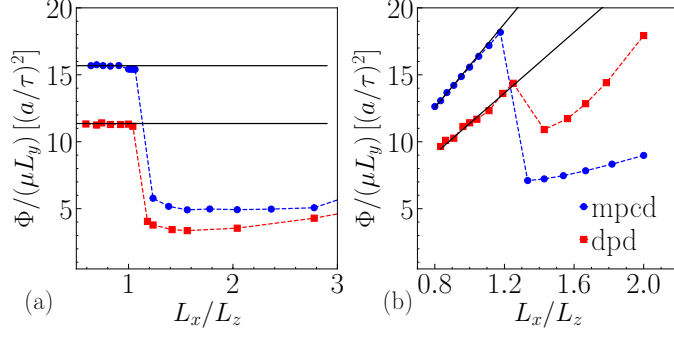


FIG. 6. (a) Total viscous dissipation  $\Phi$  as function of box shape for fixed average shear stress of  $\tau_{zx}/\mu = 0.04 \tau^{-1}$  for the MPCD fluid and  $\tau_{zx}/\mu = 0.0688 \tau^{-1}$  for the DPD fluid. (b) Total viscous dissipation for fixed maximum velocity in the exchange regions. Note that dissipation in the RNES exchange regions has been excluded from  $\Phi$  in both the numerical and theoretical calculations.

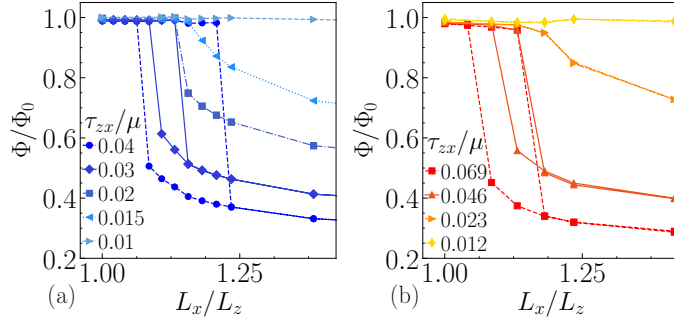


FIG. 7. Ratio of measured to expected viscous dissipation,  $\Phi/\Phi_0$ , for the (a) MPCD fluid and (b) DPD fluid in simulation boxes of varied aspect ratio,  $L_x/L_z$ , and expected shear stress,  $\tau_{zx}/\mu$ . The shear rates are indicated in the legends.

converged to the same viscous dissipation and the same flow profile. For the higher shear rates, the two systems did not converge during the length of the simulation run of  $600\,000 \tau$  for MPCD and  $70\,000 \tau$  for DPD. We therefore report both measured values of the viscous dissipation in those cases.

For both fluids and all shear rates, secondary flows formed when  $L_x/L_z > 1.25$ . The drop in the viscous dissipation was most pronounced for the biggest perturbations, even when scaled relative to  $\Phi_0$ . The viscous dissipation varied only weakly for the lowest perturbation, but weak secondary flows still developed in the elongated boxes, as shown in Fig. S4 [61]. We were unable to detect a lower critical shear rate to avoid secondary flow within the

simulation accuracy.

Because of the hysteresis, it was difficult to estimate a precise box aspect ratio for the emergence of the secondary flows. As visible in Figs. 6 and 7, boxes which were cubic or elongated in the gradient dimension ( $L_x \leq L_z$ ) always developed the expected shear flow. In contrast, simulations in boxes with  $L_x/L_z > 1.25$  always converged to a flow profile containing secondary flows. Since it can be challenging to detect the secondary flows without careful sampling of the three-dimensional velocity field, we advocate applying the RNES method for generating shear flow only when  $L_x \leq L_z$ .

## V. CONCLUSIONS

In this work, we showed that the RNES method for simulating shear flow can generate unexpected secondary flows, which do not allow a reliable calculation of the shear viscosity, in simulation boxes that are elongated in the flow dimension. We demonstrated these flows occurred over a range of box sizes and shear stresses for two different fluid models, revealing that the effect is general. Although it was challenging to precisely identify the box geometries leading to secondary flows due to hysteresis effects, we showed that no secondary flows formed during the accessible simulation time for aspect ratios,  $L_x/L_z$ , below 1.05, while they always occurred for ratios above 1.25. Weak secondary flows were obtained even for very low shear rates, indicating that there was no detectable lower threshold within the accuracy of the simulations.

The flow fields in both the cubic and elongated boxes were shown to be consistent with the same boundary condition on the average stress imposed by RNES. However, this boundary condition did not constrain the velocity along the shear gradient,  $v_z$ . When the RNES boundary conditions were augmented by hard walls to oblige  $v_z = 0$ , the secondary flows were suppressed and the expected Couette flow profile was recovered. This test demonstrated that the periodic boundary conditions of the simulation box were needed to obtain the secondary flows. For elongated simulation boxes, the fact that the RNES algorithm is compatible with periodic boundary conditions turns out to not be a feature, but rather the origin of the undesired behavior.

We measured the velocity fields to calculate the stresses and viscous dissipation. We showed that the viscous dissipation is a good predictor for the emergence of secondary



flows, with the total viscous dissipation dropping significantly compared to the theoretically expected value when the secondary flows occurred. The amount of reduction in viscous dissipation depended on the shear rate, with a greater reduction relative to the expected value at higher shear rates. We hypothesize that the secondary flows occurred because they minimized the viscous dissipation due to the flow, which is proportional to the rate of entropy generation. We speculate this behavior may be due to an underlying hydrodynamic instability with respect to the boundary conditions in this particular geometry and flow. The stability analysis of the Navier–Stokes equations for RNES is left as an intriguing subject of future work.

This study reveals a previously unappreciated limitation of the RNES method. We found that only boxes which are approximately cubic or elongated in the shear-gradient dimension can be reliably used to simulate standard shear flow, especially for higher shear rates. This has important implications for recent applications of RNES to study flow behavior of complex fluids like colloids [19, 20, 24] nanoparticles [16–18], or polymers [11, 21, 23]. Both of the fluids tested here are frequently used as background solvents in these simulations. Although it may be tempting to extend the simulation box in the flow dimension for computational efficiency, we advocate using only boxes with  $L_x \leq L_z$  to reliably generate the expected shear flow.

## ACKNOWLEDGMENTS

We thank Florian Müller-Plathe and Howard Stone for insightful discussions. We gratefully acknowledge use of computational resources supported by the Princeton Institute for Computational Science and Engineering (PICSciE) and the Office of Information Technology’s High Performance Computing Center and Visualization Laboratory at Princeton University. Financial support for this work was provided by the Princeton Center for Complex Materials, a U.S. National Science Foundation Materials Research Science and Engineering Center (award DMR-1420541), and the King Abdullah University of Science and Technology

- [1] F Müller-Plathe, “A simple nonequilibrium molecular dynamics method for calculating the thermal conductivity,” *J. Chem. Phys.* **106**, 6082–6085 (1997).
- [2] F Müller-Plathe, “Reversing the perturbation in nonequilibrium molecular dynamics: An easy way to calculate the shear viscosity of fluids,” *Phys. Rev. E* **59**, 4894 (1999).
- [3] D Reith and F Müller-Plathe, “On the nature of thermal diffusion in binary Lennard-Jones liquids,” *J. Chem. Phys.* **112**, 2436–2443 (2000).
- [4] J Ding, G Pan, L Du, J Lu, W Wang, X Wei, and J Li, “Molecular dynamics simulations of the local structures and transport properties of  $\text{Na}_2\text{CO}_3$  and  $\text{K}_2\text{CO}_3$ ,” *Applied Energy* **227**, 555 – 563 (2018).
- [5] M Alaghemandi, E Algaer, M C Böhm, and F Müller-Plathe, “The thermal conductivity and thermal rectification of carbon nanotubes studied using reverse non-equilibrium molecular dynamics simulations,” *Nanotechnology* **20**, 115704 (2009).
- [6] MA Osman and D Srivastava, “Temperature dependence of the thermal conductivity of single-wall carbon nanotubes,” *Nanotechnology* **12**, 21 (2001).
- [7] MS El-Genk, K Talaat, and BJ Cowen, “Thermal conductivity of silicon using reverse non-equilibrium molecular dynamics,” *J. Appl. Phys.* **123**, 205104 (2018).
- [8] M Zhang and F Müller-Plathe, “Reverse nonequilibrium molecular-dynamics calculation of the Soret coefficient in liquid benzene/cyclohexane mixtures,” *J. Chem. Phys.* **123**, 124502 (2005).
- [9] T Soddemann, B Dünweg, and K Kremer, “Dissipative particle dynamics: A useful thermostat for equilibrium and nonequilibrium molecular dynamics simulations,” *Phys. Rev. E* **68**, 046702 (2003).
- [10] H Guo, K Kremer, and T Soddemann, “Nonequilibrium molecular dynamics simulation of shear-induced alignment of amphiphilic model systems,” *Phys. Rev. E* **66**, 061503 (2002).
- [11] A Nikoubashman and MP Howard, “Equilibrium Dynamics and Shear Rheology of Semiflexible Polymers in Solution,” *Macromolecules* **50**, 8279–8289 (2017).
- [12] P V Ramírez-González and V A Escobar-Barrios, “Viscosity and normal stress forces of Lennard-Jones chains using reverse non-equilibrium molecular dynamics,” *Mol. Phys.* **115**,

- 2970–2977 (2017).
- [13] MS Kelkar and EJ Maginn, “Effect of temperature and water content on the shear viscosity of the ionic liquid 1-ethyl-3-methylimidazolium bis (trifluoromethanesulfonyl) imide as studied by atomistic simulations,” *J. Phys. Chem. B* **111**, 4867–4876 (2007).
  - [14] MS Kelkar, JL Rafferty, EJ Maginn, and JI Siepmann, “Prediction of viscosities and vapor–liquid equilibria for five polyhydric alcohols by molecular simulation,” *Fluid Phase Equilib.* **260**, 218–231 (2007).
  - [15] M Yijin and Z Yuwen, “Thermal conductivity, shear viscosity and specific heat of rigid water models,” *Chem. Phys. Lett.* **542**, 37 – 41 (2012).
  - [16] W Zhao, F Leroy, S Balasubramanian, and F Müller-Plathe, “Shear Viscosity of the Ionic Liquid 1-n-Butyl 3-Methylimidazolium Hexafluorophosphate [bmim][PF<sub>6</sub>] Computed by Reverse Nonequilibrium Molecular Dynamics,” *J. Phys. Chem. B* **112**, 8129–8133 (2008).
  - [17] A Sambasivam, S Dhakal, and R Sureshkumar, “Structure and rheology of self-assembled aqueous suspensions of nanoparticles and wormlike micelles,” *Mol. Sim.* **44**, 485–493 (2018).
  - [18] DR Heine, MK Petersen, and GS Grest, “Effect of particle shape and charge on bulk rheology of nanoparticle suspensions,” *J. Chem. Phys.* **132**, 184509 (2010).
  - [19] M Cerbelaud, A Maria Laganapan, T Ala-Nissila, R Ferrando, and A Videcoq, “Shear viscosity in hard-sphere and adhesive colloidal suspensions with reverse non-equilibrium molecular dynamics,” *Soft Matter* **13**, 3909–3917 (2017).
  - [20] JD Olarte-Plata and F Bresme, “Microscopic relationship between colloidcolloid interactions and the rheological behaviour of suspensions: a molecular dynamics-stochastic rotation dynamics investigation,” *Mol. Phys.* **0**, 1–9 (2018).
  - [21] S Meng, J Zhang, Y Wang, X Li, C Wu, T Hou, L Xiao, and G Lu, “Simulating the rheology of surfactant solution using dissipative particle dynamics,” *Mol. Sim.* **41**, 772–778 (2015).
  - [22] H Yao, Q Dai, and Z You, “Molecular dynamics simulation of physicochemical properties of the asphalt model,” *Fuel* **164**, 83 – 93 (2016).
  - [23] L Schneider, M Heck, M Wilhelm, and M Müller, “Transitions between Lamellar Orientations in Shear Flow,” *Macromolecules* **51**, 4642–4659 (2018).
  - [24] R D Mountain, W H Hatch, and V K Shen, “Molecular dynamics simulation of trimer self-assembly under shear,” *Fluid Phase Equilib.* **440**, 87 – 94 (2017).
  - [25] W G Hoover, “Nonequilibrium Molecular Dynamics,” *Ann. Rev. Phys. Chem.* **34**, 103–127

- (1983).
- [26] F Müller-Plathe and P Bordat, “Reverse non-equilibrium molecular dynamics,” in *Novel Methods in Soft Matter Simulations*, edited by Mikko Karttunen, Ari Lukkarinen, and Ilpo Vattulainen (Springer Berlin Heidelberg, Berlin, Heidelberg, 2004) pp. 310–326.
  - [27] R Zwanzig, “Time-correlation functions and transport coefficients in statistical mechanics,” *Ann. Rev. Phys. Chem.* **16**, 67–102 (1965).
  - [28] J W Perram and L R White, “Structure of the Liquid/Vapour and Liquid/Solid Interfaces,” *Faraday Discuss. Chem. Soc.* **59**, 29–37 (1975).
  - [29] Denis J Evans and Gary P Morris, “Shear Thickening and Turbulence in Simple Fluids,” *Phys. Rev. Lett.* **56**, 2172–2175 (1986).
  - [30] S Plimpton, “Fast Parallel Algorithms for Short-Range Molecular Dynamics,” *J. Comput. Phys.* **117**, 1 – 19 (1995).
  - [31] J A Anderson, C D Lorenz, and A Travesset, “General purpose molecular dynamics simulations fully implemented on graphics processing units,” *J. Comput. Phys.* **227**, 5342 – 5359 (2008).
  - [32] P Louden, H Bhattarai, S Neidhart, T Lin, Charles F Vardeman II, C J Fennell, MA Meineke, S Kuang, M Lamichhane, J Michalka, *et al.*, “OPENMD-2.5: Molecular Dynamics in the Open,” (2017).
  - [33] HJ Limbach, A Arnold, BA Mann, and C Holm, “ESPRessoan extensible simulation package for research on soft matter systems,” *Comput. Phys. Commun.* **174**, 704–727 (2006).
  - [34] W M Deen, *Analysis of Transport Phenomena, Topics in Chemical Engineering*, 2nd ed. (Oxford University Press, New York, 2012).
  - [35] CM Tenney and EJ Maginn, “Limitations and recommendations for the calculation of shear viscosity using reverse nonequilibrium molecular dynamics,” *J. Chem. Phys.* **132**, 014103 (2010).
  - [36] CP Calderon and WT Ashurst, “Comment on ”Reversing the perturbation in nonequilibrium molecular dynamics: An easy way to calculate the shear viscosity of fluids”,” *Phys. Rev. E* **66**, 013201 (2002).
  - [37] M K Petersen, J B Lechman, S J Plimpton, G S Grest, P J in t Veld, and P R Schunk, “Mesoscale hydrodynamics via stochastic rotation dynamics: Comparison with Lennard-Jones fluid,” *J. Chem. Phys.* **132**, 174106 (2010).

- [38] MP Allen and DJ Tildesley, *Computer simulation of liquids* (Oxford university press, 2017).
- [39] M Doi and S F Edwards, *The theory of polymer dynamics* (Oxford university press, 1988).
- [40] A Malevanets and R Kapral, “Mesoscopic model for solvent dynamics,” *J. Chem. Phys.* **110**, 8605–8613 (1999).
- [41] G Gompper, T Ihle, D M Kroll, and R G Winkler, “Multi-Particle Collision Dynamics: A Particle-Based Mesoscale Simulation Approach to the Hydrodynamics of Complex Fluids,” in *Advanced Computer Simulation Approaches for Soft Matter Sciences III*, edited by C Holm and K Kremer (Springer Berlin Heidelberg, Berlin, Heidelberg, 2009) pp. 1–87.
- [42] PJ Hoogerbrugge and JMVA Koelman, “Simulating microscopic hydrodynamic phenomena with dissipative particle dynamics,” *Europhys. Lett.* **19**, 155 (1992).
- [43] AG Schlijper, PJ Hoogerbrugge, and CW Manke, “Computer simulation of dilute polymer solutions with the dissipative particle dynamics method,” *J. Rheol.* **39**, 567–579 (1995).
- [44] RD Groot and PB Warren, “Dissipative particle dynamics: Bridging the gap between atomistic and mesoscopic simulation,” *J. Chem. Phys.* **107**, 4423–4435 (1997).
- [45] H Noguchi, N Kikuchi, and G Gompper, “Particle-based mesoscale hydrodynamic techniques,” *Europhys. Lett.* **78**, 10005 (2007).
- [46] T Ihle and D M Kroll, “Stochastic rotation dynamics: A Galilean-invariant mesoscopic model for fluid flow,” *Phys. Rev. E* **63**, 020201(R) (2001).
- [47] T Ihle and D M Kroll, “Stochastic rotation dynamics. I. Formalism, Galilean invariance, and Green-Kubo relations,” *Phys. Rev. E* **67**, 066705 (2003).
- [48] R Kapral, “Multiparticle Collision Dynamics: Simulation of Complex Systems on Mesoscales,” in *Advances in Chemical Physics* (Wiley-Blackwell, 2008) pp. 89–146.
- [49] C.-C. Huang, A Varghese, G Gompper, and RG Winkler, “Thermostat for nonequilibrium multiparticle-collision-dynamics simulations,” *Phys. Rev. E* **91**, 013310 (2015).
- [50] C.C. Huang, A. Chatterji, G. Sutmann, G. Gompper, and R.G. Winkler, “Cell-level canonical sampling by velocity scaling for multiparticle collision dynamics simulations,” *J. Comput. Phys.* **229**, 168 – 177 (2010).
- [51] M Ripoll, K Mussawisade, RG Winkler, and G Gompper, “Dynamic regimes of fluids simulated by multiparticle-collision dynamics,” *Phys. Rev. E* **72**, 016701 (2005).
- [52] JMVA Koelman and PJ Hoogerbrugge, “Dynamic simulations of hard-sphere suspensions under steady shear,” *Europhys. Lett.* **21**, 363 (1993).

- [53] MB Liu, GR Liu, LW Zhou, and JZ Chang, “Dissipative Particle Dynamics (DPD): An Overview and Recent Developments,” *Archives of Computational Methods in Engineering* **22**, 529–556 (2015).
- [54] J. A. Backer, C. P. Lowe, H. C. J. Hoefsloot, and P. D. Iedema, “Poiseuille flow to measure the viscosity of particle model fluids,” *The Journal of Chemical Physics* **122**, 154503 (2005).
- [55] A. Boromand, S. Jamali, and J. M. Maia, “Viscosity measurement techniques in Dissipative Particle Dynamics,” *Computer Physics Communications* **196**, 149 – 160 (2015).
- [56] J Glaser, TD Nguyen, JA Anderson, P Lui, F Spiga, JA Millan, DC Morse, and SC Glotzer, “Strong scaling of general-purpose molecular dynamics simulations on GPUs,” *Comput. Phys. Commun.* **192**, 97 – 107 (2015).
- [57] M P Howard, A Z Panagiotopoulos, and A Nikoubashman, “Efficient mesoscale hydrodynamics: multiparticle collision dynamics with massively parallel GPU acceleration,” *Comput. Phys. Commun.* **230**, 10–20 (2018).
- [58] CL Phillips, JA Anderson, and SC Glotzer, “Pseudo-random number generation for Brownian Dynamics and Dissipative Particle Dynamics simulations on GPU devices,” *J. Comput. Phys.* **230**, 7191 – 7201 (2011).
- [59] Arash Nikoubashman, private communication (2018).
- [60] <https://lammps.sandia.gov/>.
- [61] See Supplemental Material at <http://XXX> for additional information..
- [62] SA Orszag and LC Kells, “Transition to turbulence in plane Poiseuille and plane Couette flow,” *J. Fluid Mech.* **96**, 159205 (1980).
- [63] BJ Bayly, SA Orszag, and T Herbert, “Instability Mechanisms in Shear-Flow Transition,” *Ann. Rev. Fluid Mech.* **20**, 359–391 (1988).
- [64] A Lundbladh and AV Johansson, “Direct simulation of turbulent spots in plane Couette flow,” *J. Fluid Mech.* **229**, 499516 (1991).
- [65] D. S. Bolintineanu, J. B. Lechman, S. J. Plimpton, and G. S. Grest, “No-slip boundary conditions and forced flow in multiparticle collision dynamics,” *Phys. Rev. E* **86**, 066703 (2012).
- [66] Antonio Lamura, Gerhard Gompper, Thomas Ihle, and DM Kroll, “Multi-particle collision dynamics: Flow around a circular and a square cylinder,” *Europhys. Lett.* **56**, 319 (2001).
- [67] CL Iandoli and Enrico Sciubba, “3-D numerical calculation of the local entropy generation

rates in a radial compressor stage,” *Int. J. Thermodyn.* **8**, 83–94 (2005).